



Bimetallic Pd–Cu catalysts for selective CO₂ hydrogenation to methanol

Xiao Jiang^{a,b}, Naoto Koizumi^a, Xinwen Guo^c, Chunshan Song^{a,b,c,*}

^a Clean Fuels & Catalysis Program, PSU–DUT Joint Center for Energy Research, EMS Energy Institute, The Pennsylvania State University, 209 Academic Projects Building, University Park, PA 16802, USA

^b John and Willie Leone Family Department of Energy and Mineral Engineering and Department of Chemical Engineering, The Pennsylvania State University, University Park, PA 16802, USA

^c PSU–DUT Joint Center for Energy Research, State Key Laboratory of Fine Chemicals, School of Chemical Engineering, Dalian University of Technology, Dalian 116024, China

ARTICLE INFO

Article history:

Received 5 July 2014

Received in revised form

29 December 2014

Accepted 9 January 2015

Available online 12 January 2015

Keywords:

CO₂ hydrogenation

Pd–Cu bimetallic catalyst

Methanol

Pd–Cu alloy formation

Support effect

ABSTRACT

This paper reports on novel Pd–Cu bimetallic catalysts for selective CO₂ hydrogenation to methanol. Strong synergistic effect on promoting methanol formation was observed over amorphous silica supported Pd–Cu bimetallic catalysts when the Pd/(Pd + Cu) atomic ratios lied in the range of 0.25–0.34. The methanol formation rate over Pd(0.25)–Cu/SiO₂ was two times higher than the simple sum of those over monometallic Cu and Pd catalysts. The Pd–Cu bimetallic catalysts were characterized by X-ray diffraction, transmission electron microscopy, scanning transmission electron microscopy coupled with energy dispersive X-ray spectroscopy, X-ray photoelectron spectroscopy, and hydrogen temperature-programmed desorption. Detailed characterization results demonstrated the importance of two well-dispersed Pd–Cu alloy particles (PdCu and PdCu₃) for the observed methanol promotion over Pd–Cu bimetallic catalysts. Similar bimetallic promotion was also observed for Pd–Cu catalysts supported on uniform mesoporous MCM-41, SBA-15 and MSU-F. Conversion-selectivity profile of the Pd–Cu/SiO₂ catalyst suggested that CO₂ was a primary carbon source for methanol synthesis at lower CO₂ conversion, and byproduct CO contributed at higher CO₂ conversion within the conversion range examined.

© 2015 Elsevier B.V. All rights reserved.

1. Introduction

Utilization of CO₂ as a carbon source for synthesizing chemical feedstocks and transportation fuels has recently attracted great attention worldwide [1–13], because a major advance in energy-efficient catalytic CO₂ conversion using renewable energy could reduce both the greenhouse-gas emissions and the dependence on nonrenewable resources such as petroleum. The synthesis of oxygenates and hydrocarbons from CO₂ hydrogenation using hydrogen produced with renewable energy such as solar energy, is one of the promising approaches for the environmentally-friendly synthesis of sustainable chemical feedstocks and fuels.

Methanol (CH₃OH) is an important chemical feedstock and can also be used as a fuel for internal combustion engines and fuel cells.

Over the past two decades, significant efforts have been devoted to developing effective catalysts for CO₂ hydrogenation to CH₃OH. These previous studies focused mainly on improving the activity and selectivity of Cu–Zn based catalysts by, e.g., exploring effective promoters and supports, or developing new preparation methods [14–26]. For the Cu–Zn system, Zn is well known as an effective promoter. Fujitani and Nakamura [27] studied mechanistic aspects of the role of the Zn promoter using a Zn doped Cu(1 1 1) model catalyst, demonstrating that the addition of Zn to the Cu surface formed Cu–Zn alloy that decreased the stability of adsorbed formate species, which the authors considered as a crucial intermediate for CH₃OH formation. However, Cu–Zn based catalysts require higher temperatures for CO₂ hydrogenation at adequate rates, while hydrogenation to CH₃OH is favorable thermodynamically at lower temperatures. At the typical reaction condition for the Cu–Zn catalyst (573 K and 4.1 MPa), the equilibrium yield of CH₃OH is only 14%.

Several researchers have reported that Pd nanoparticles supported on metal oxides possess the ability to hydrogenate CO₂ to CH₃OH [28–35]. Supported Pd nanoparticles have been reported to

* Corresponding author at: Clean Fuels & Catalysis Program, PSU–DUT Joint Center for Energy Research, EMS Energy Institute, The Pennsylvania State University, 209 Academic Projects Building, University Park, PA 16802, USA. Tel.: +1 8148634466; fax: +1 8148653573.

E-mail address: csong@psu.edu (C. Song).

be active for CH_3OH formation from CO hydrogenation [36–39]. CeO_2 supported Pd catalysts showed excellent activities for CO hydrogenation to CH_3OH even at low temperatures where Cu–ZnO based catalysts did not work well [37]. We have recently shown that nano-structured Pd catalysts with enhanced activities for CO_2 hydrogenation to CH_3OH can be prepared by combining two different strategies, namely incorporation of uniform mesoporous supports such as MCM-41 and SBA-15 leading to small Pd nanoparticles inside nano-sized pore channels, and promotion by alkali/alkaline earth metal additives [40]. K(Ca)-promoted Pd supported on SBA-15 yielded 2–5 times more methanol than an amorphous silica supported Pd catalyst. However, current Pd catalysts yield much smaller amounts of CH_3OH from CO_2 hydrogenation compared to the Cu–Zn based catalysts [32], although the Pd catalysts would be a potential candidate for low-temperature CH_3OH synthesis using CO_2 .

In addition to Cu-based and Pd-based catalysts, it has been reported that the metallic Cu–Ni alloy surface is active for CO/CO_2 hydrogenation to CH_3OH [41,42]. In this context, it is interesting to clarify if Pd and Cu combination could result in more active catalysts for CO_2 hydrogenation to methanol. It is known that Pd and Cu can form stable alloy after reduction [43,44]. Moreover, apart from Cu–Zn alloy, Pd–Cu alloy may promote CH_3OH formation. Therefore, it would be of great interest to see if the Pd–Cu alloys with different compositions promote CO_2 hydrogenation, not only for exploring new CH_3OH synthesis catalysts, but also for understanding the chemistry in CH_3OH formation on the metallic alloy surface. Previous work showed that Pd–Cu bimetallic catalysts were active for hydrogenation of unsaturated organic compounds [45–47] and oxygen-enhanced water–gas shift reaction [48,49]. However, to our knowledge, little has been reported on the Pd–Cu bimetallic catalyst for CO_2 hydrogenation to CH_3OH .

The aim of this work is to explore the catalytic properties of Pd–Cu bimetallic catalysts for CO_2 hydrogenation to methanol. A series of supported Pd–Cu catalysts with a wide range of Pd and Cu loadings were prepared using amorphous silica and uniform mesoporous silica (SBA-15, MCM-41, and MSU-F) as supports. CO_2 hydrogenation activity and selectivity over these bimetallic catalysts were investigated under pressurized condition and also compared to those over Cu–ZnO counterparts. In order to examine the structure–activity relationship for Pd–Cu catalysts, these catalysts were also characterized by powder X-ray diffraction (XRD), transmission electron microscopy (TEM), scanning transmission electron microscopy/energy dispersive X-ray spectroscopy (STEM/EDS), X-ray photoelectron spectroscopy (XPS), and temperature programmed desorption of hydrogen (H_2 -TPD).

2. Experimental

2.1. Preparation of catalysts

Amorphous silica (Davisil Grade 62, particle size = $75\text{--}250 \times 10^{-6}\text{ m}$) was used as support. MCM-41 and SBA-15 were prepared according to the procedures reported previously [50–52]. MSU-F is a mesoporous silica (purchased from Aldrich) with hexagonal and cellular foam-like structure containing large pores and well cross-lined framework walls.

Amorphous silica supported Pd–Cu bimetallic catalysts were prepared by coimpregnation method using acetone solution of $\text{Pd}(\text{CH}_3\text{COO})_2$ (Aldrich, >99.9%) and $\text{Cu}(\text{NO}_3)_2 \cdot 2.5\text{H}_2\text{O}$ (Alfa Aesar, ≥98%) [53]. The impregnated samples were dried at ambient temperature and calcined in an electric furnace at 723 K for 5 h under flowing dry air (ca. $100\text{ mL (NTP) min}^{-1}$). The Cu/(Pd + Cu) atomic ratios were varied in the range of 0.0–0.94, and Pd/(Pd + Cu) atomic

ratios ranged from 0.0 to 0.60. To investigate Cu loading effect, the Pd loading was fixed at 5.7 wt% initially to compare with our early work [40]. Coimpregnation method was also used for preparing Pd–Cu supported on uniform mesoporous silica (ca. SBA-15, MCM-41, and MSU-F).

For comparison, Pd–Cu bimetallic catalysts were also prepared by sequential impregnation onto amorphous silica using acetone solutions of the same precursors with different impregnation sequences while keeping the composition of the catalysts identical to the coimpregnated sample. The precursor for Pd (or Cu) was impregnated first and dried at ambient temperature, followed by impregnation of the precursor for Cu (or Pd) without an intermediate calcination. The sequentially impregnated Pd–Cu samples were calcined at the same condition as that for coimpregnated samples.

For comparison, supported monometallic Pd and Cu catalysts were prepared as well. As benchmark, amorphous silica supported Cu–Zn catalysts and commercial Cu–ZnO– Al_2O_3 catalyst (MDC-3, Süd-Chemie, 40 wt% Cu, 20–32 meshes) were also tested. Amorphous silica supported Cu–Zn bimetallic catalysts were prepared using $\text{Zn}(\text{NO}_3)_2 \cdot 6\text{H}_2\text{O}$ (Alfa Aesar, 99.998%) as the Zn source at a fixed Cu loading of 10 wt% (support weight basis). The Zn/(Zn + Cu) atomic ratio ranged from 0.0 to 0.80.

The bimetallic catalysts prepared by coimpregnation are denoted as Pd(X)–Cu(Y)/support and Cu–ZnO(Z)/ SiO_2 , where X, Y, and Z represent Pd/(Pd + Cu), Cu/(Pd + Cu), and Zn/(Zn + Cu) atomic ratios, respectively. Monometallic catalysts are denoted as Pd/support and Cu/support, and the metal loadings of Pd and Cu are 5.7 wt% and 10 wt%, respectively, unless otherwise noted. The catalysts with a hyphen (–) between two metals are prepared by coimpregnation method; in contrast, the samples with a slash (/) between metals are prepared by sequential impregnation method, and the metal next to support in the denotation is impregnated first.

2.2. Catalytic test

The prepared catalysts were tested under pressurized condition using a fixed bed reactor system consisting of a stainless steel tube with an internal diameter of 6 mm placed in an electrically heated oven. The gases, H_2 (99.995%) and 24 vol% $\text{CO}_2/72\text{ vol}\% \text{H}_2/4\text{ vol}\% \text{Ar}$ (99.995%), were used without further purification. The flow rate and pressure of these gases were regulated with mass flow controllers and a backpressure regulator, respectively. The amount of catalyst used in a typical run was 0.20 g. The amorphous silica supported catalysts were diluted by inert amorphous silica particles ($\sim 0.42\text{ g}$) of the same size to attain aspect ratio of approximately 6.0; while other mesoporous silica supported catalysts with low densities (such as SBA-15, MCM-41, and MSU-F) were not diluted. The catalysts were heated up to 573 K in a stream of H_2 at a ramp rate of 2.3 K min^{-1} and then maintained under isothermal condition (573 K) for 2 h. After H_2 reduction, the temperature was reduced to ambient temperature. The feed gas $\text{CO}_2/\text{H}_2/\text{Ar}$ was then employed to pressurize the system to 4.1 MPa (GHSV = $3600\text{ mL(STP) g-cat}^{-1}\text{ h}^{-1}$) and the reactor system was heated to desired temperature at a ramp rate of 1.9 K min^{-1} for the catalytic reaction.

Gaseous products were periodically sampled with computer-controlled gas samplers and analyzed by two online GCs (SRI 8610C). An online GC/TCD was used to analyze Ar, CO and CO_2 , while the other online GC/FID was for CH_3OH and CH_4 . Ar was an internal standard to estimate CO_2 conversion, and CH_4 was employed as an external standard for measuring methanol formation rate. The accuracy of the experimental data was ensured by five separate runs over Pd(0.34)–Cu/ SiO_2 catalyst, which showed maximum CH_3OH formation rate. The standard deviations for CO_2 conversion, CH_3OH formation rate, and CO formation rate were

0.2%, 0.02 $\mu\text{mol g}^{-1} \text{s}^{-1}$, and 0.01 $\mu\text{mol g}^{-1} \text{s}^{-1}$, respectively.

2.3. Passivation of reduced/spent catalysts

Reduced and spent catalysts were passivated in 0.970 vol% $\text{O}_2/99.030 \text{ vol}\% \text{ He}$ (99.995%) at ambient temperature for 4 h. The flow rate was controlled at about 20 mL (STP) min^{-1} . The catalysts were then collected for characterization, hereafter simply denoted as reduced or spent catalysts.

2.4. Characterization of catalysts

The N_2 adsorption–desorption isotherms for catalysts and supports were measured in a Micromeritics ASAP 2020 equipment. The samples were degassed at 523 K for 12 h prior to analysis. Specific surface areas were estimated using the BET method. Pore size distributions were obtained by applying the B.J.H. formalism to the desorption branch of the isotherms.

XRD patterns of the catalysts were collected using a PANalytical Empyrean X-Ray Diffractometer with $\text{Cu K}\alpha$ ($\lambda = 0.154059 \text{ nm}$) radiation, and fixed slit incidence (0.25° divergence, 0.5° anti-scatter, specimen length 10 mm) and diffracted (0.25° anti-scatter, 0.02 mm nickel filter) optics. Samples were prepared by the back-loading method in which a powder sample is pressed into the cavity of a quartz zero-background support. Data was collected at 45 kV and 40 mA from 30 to 90° (2θ) using a PIXcel detector in scanning mode and 255 active channels for a duration time of $\sim 20 \text{ min}$. Resulting patterns were corrected for both 2θ position and instrumental peak broadening using NIST (National Institute of Standards and Technology) 640c silicon and analyzed with Jade+9 software by MDI of Livermore, CA. All of the XRD patterns were replotted after background subtraction and curve fitting. The crystal sizes of different metal phases in the samples were determined from the full width at half maximum (FWHM) of the (1 1 1) peaks using Scherrer equation

$$D = \frac{K \times \lambda}{\beta \times \cos \theta} \quad (1)$$

where K is a dimensionless shape factor, with a value close to unity, λ is the X-ray wavelength (0.154059 nm), θ is the Bragg angle, D is the mean size of ordered crystalline domains, and β is the FWHM in radians after correction.

The reduced Pd–Cu bimetallic catalysts were analyzed by transmission electron microscopy (TEM, Tecnai G220 S-Twin, 200 kV, FEI Company). Reduced samples were first collected after passivation as described in Section 2.3 and then ultrasonicated in ethanol. A few droplets of ethanol suspension were dropped onto a carbon-coated copper grid and followed by drying at ambient temperature. Typically about 30 micrographs were taken for each sample. Alloy Pd–Cu particle size histograms were generated by counting at least 150 particles.

The morphological properties of reduced Pd–Cu bimetallic catalysts were also studied by scanning transmission electron microscopy/energy-dispersive X-ray spectroscopy (STEM/EDS) using a FEI Titan G2 TEM equipped with a spherical aberration corrector on the probe-forming lens at an accelerating voltage of 300 kV. EDS maps were acquired in the Titan using ChemiSTEM quad detectors at a current of 0.12 nA for 10 min. Standardless Cliff–Lorimer quantification was done on the deconvoluted EDS line intensity data using the Bruker Esprit software. The sample preparation procedure was very similar to TEM samples. Carbon-coated molybdenum grid was applied to avoid the interference from Cu in both mapping and quantifying.

X-ray photoelectron spectra (XPS) were acquired on a Kratos Axis Ultra using monochromatic $\text{Al-K}\alpha$ radiation (1486.6 eV). The

anode voltage and current were 14 keV and 20 mA, respectively. Analytical chamber pressures were in the low 10^{-8} torr range during data acquisition. All spectra were acquired in hybrid slot mode, with the charge-neutralizer on. The neutralizer filament current was set at 2.2 amps, while the charge balance and filament bias settings were 1 V and 3 V, respectively. High resolution spectra were acquired at a pass energy of 40 eV, with a step size of 0.2 eV. A dwell time of 2500 ms was used for the Cu 2p, C 1s, and Pd 3d peaks. The dwell times for the O 1s and Si 2p peaks were 800 and 1500 ms, respectively. Survey spectra were acquired at a pass energy of 80 eV, with 0.5 eV steps, and a 150 ms dwell time. All spectra were acquired in one sweep. The analysis area was roughly 1 mm in diameter. Transmission function corrections were provided by the Kratos software, and all data were processed with CASA XPS, using the following RSF values: Pd 3d (5.323), Cu 2p $_{3/2}$ (3.134), Si 2p (0.303), C 1s (0.297), and O 1s (0.703). The BE scale was calibrated using the BEs of Au 4f $_{7/2}$, Ag 3d $_{5/2}$, and Cu 2p $_{3/2}$ at 83.96, 368.21, and 932.62 eV, respectively. All spectra were charge corrected to Si 2p at 103.5 eV (see Supplementary information). All samples, including bare support silica, were reduced under the same conditions, with subsequent passivation. Surface carbon was detected in all samples, and included in the calculation of surface composition. The atomic concentrations of palladium, copper, silicon, carbon, and oxygen were calculated from peak areas obtained from the high-resolution spectra, using a Shirley background subtraction.

Hydrogen temperature-programmed desorption (H_2 -TPD) was carried out on an Autochem 2910 TPD/TPR equipped with a TCD detector. Ametek Dycor Dymaxion mass spectrometer DM200M was employed for monitoring the real-time concentrations of desorbed hydrogen. The calcined catalyst ($\sim 150 \text{ mg}$) was reduced in situ in H_2 at 573 K for 2 h and then allowed to cool down to 303 K, followed by flushing the catalyst bed with 1 vol% $\text{Ar}/99 \text{ vol}\% \text{ He}$ (30 mL min^{-1}) at the ambient temperature and the TPD experiment with heating up to 1173 K at a ramp rate of 10 K min^{-1} .

3. Results and discussion

3.1. Effect of combining Pd and Cu on CO_2 hydrogenation

3.1.1. Effects of Pd and Cu loadings

To identify the effect of Cu and Pd loadings, two series of the amorphous silica supported Pd–Cu bimetallic catalysts with different metal loadings, Pd(X)–Cu/SiO $_2$ and Pd–Cu(Y)/SiO $_2$, were tested for CO_2 hydrogenation at 523 K and 4.1 MPa. This is the same condition as in our early work [40] for comparison. These bimetallic catalysts yielded only CO and CH_3OH as carbon-containing products. Both CO_2 conversion and products formation rates were practically constant from 5 h to 100 h on stream. Thus, the activity and selectivity of the bimetallic catalysts reported here were collected at 10–12 h on stream.

Fig. 1A illustrates the changes in the CO_2 conversion and product formation rate over Pd–Cu(Y)/SiO $_2$ catalysts as a function of the Cu/(Pd + Cu) atomic ratio. The ratio was varied by changing Cu loading from 0 to 50 wt%. The Pd loading was initially fixed at 5.7 wt% based on our previous work [40]. CO_2 conversion on monometallic Pd catalyst is 3%. Only a small amount of CH_3OH was obtained in the product stream and this catalyst yields CO selectively. The CO_2 conversion increased gradually with increasing Cu loading and maximized at Cu/(Pd + Cu) ratio of 0.9. The formation rate of CO changed in a similar way; however, CH_3OH formation rate maximized at slightly lower Cu/(Pd + Cu) atomic ratio, which is 0.75 (Cu loading 10 wt%). Therefore, 10 wt% Cu loading was employed hereafter in this work.

Table 1
CO₂ hydrogenation activity and product selectivity over supported Pd–Cu and Cu–Zn catalysts.^{a,b}

Support	Active metals	CO ₂ conv./%	Product selectivity/mol%		Formation rate of products/ $\mu\text{mol g-cat}^{-1} \text{s}^{-1}$	
			CO	CH ₃ OH	CO	CH ₃ OH
SiO ₂	Pd	3.0	77	23	0.29	0.09
	Cu	2.8	85	15	0.27	0.05
	Pd(0.25)–Cu	6.7	70	30	0.65	0.28
	Pd(0.34)–Cu	6.6	66	34	0.61	0.31
	Pd(0.34)/Cu ^c	5.0	77	23	0.50	0.16
	Cu/Pd(0.34) ^c	4.9	76	24	0.50	0.15
MCM-41	Pd	<1	–	–	0.02	<0.01
	Cu	<1	60	40	0.03	0.02
	Pd(0.25)–Cu	6.2	77	23	0.61	0.18
SBA-15	Pd	<1	–	–	0.01	<0.01
	Cu	1.5	88	12	0.21	0.03
	Pd(0.25)–Cu	6.5	77	23	0.67	0.20
MSU-F	Pd	<1	86	14	0.11	0.02
	Cu	<1	82	18	0.13	0.03
	Pd(0.25)–Cu	5.3	82	18	0.50	0.11
Cu–Zn(0.67)/SiO ₂ ^d	–	2.2	50	50	0.12	0.12
Cu–ZnO–Al ₂ O ₃ ^e	–	18.4	73	27	1.26	0.48

^a Reaction conditions: 523 K, 4.1 MPa, GHSV = 3600 mL(STP) g-cat^{−1} h^{−1}.

^b Most catalysts were prepared by coimpregnation method, unless specially noted. For monometallic and bimetallic catalyst, Pd and Cu metal loadings were 5.7 wt% and 10 wt%, respectively.

^c Catalysts were prepared by sequential impregnation method. Cu loading was 10 wt%.

^d Catalysts were prepared by coimpregnation method. Cu loading was 10 wt%.

^e MDC-3 commercial catalyst (Cu loading = 40 wt%), 20–32 meshes.

The effect of combining Pd and Cu was also investigated with different Pd/(Pd + Cu) atomic ratios while keeping Cu loading constant at 10 wt%. As illustrated in Fig. 1B, the trends of both CO and CH₃OH formation rates exhibited a volcano-like shape with the rise of Pd/(Pd + Cu) atomic ratio, and CH₃OH maximizes in the range of 0.25–0.34 (Pd loading 5.7–8.7 wt%). Within this range, Pd(0.34)–Cu/SiO₂ yielded 0.31 $\mu\text{mol g-cat}^{-1} \text{s}^{-1}$ of CH₃OH, which is 6 times more than monometallic Cu/SiO₂ with the same Cu loading and the CH₃OH selectivity was also doubled from 15 mol% to 34 mol%. The optimum Pd/(Pd + Cu) atomic ratio appears to be 0.34, which corresponds to metal loadings of 8.7 wt% Pd and 10 wt% Cu in Pd–Cu/SiO₂ catalyst. In addition, it is noticeable that the maximum values of CO and CH₃OH formation rates correspond to different atomic ratios, implying other possible carbon source for CH₃OH formation apart from CO₂ directly. This will be discussed later.

Table 1 summarizes the CO₂ hydrogenation activity and selectivity of Pd(0.25)–Cu/SiO₂ catalyst in comparison to those of monometallic Pd/SiO₂ and Cu/SiO₂ catalysts with comparable metal loadings. The properties of the catalysts are shown in Table 2.

The formation rate of CH₃OH on the bimetallic catalyst is 2 times as much as the sum of those over monometallic catalysts, indicating a significant bimetallic promotion on CH₃OH formation from CO₂ hydrogenation. For comparison, sequentially impregnated bimetallic catalysts were also tested. As shown in Table 1, Pd/Cu and Cu/Pd catalysts show almost identical activities, and both are more active than monometallic catalysts. However, neither one shows comparable methanol formation rate nor selectivity compared to coimpregnated samples with the same metal loadings. XRD results (Figs. 4 and 5, and S4) reveal that the formation of alloy phases is sensitive to impregnation method (coimpregnation vs sequential impregnation), and affects activity. However, the specific order of the sequential impregnation has little impact on the formation of alloy phases, thus leading to identical activity of the two catalysts. Due to the superior CH₃OH formation rate, coimpregnation method was used in the preparing most bimetallic catalysts throughout the present work, except for the comparison of preparation methods.

Fig. 2 demonstrates the good stabilities of CO₂ conversion and product formation rates over Pd(0.34)–Cu/SiO₂. Both CO₂ conver-

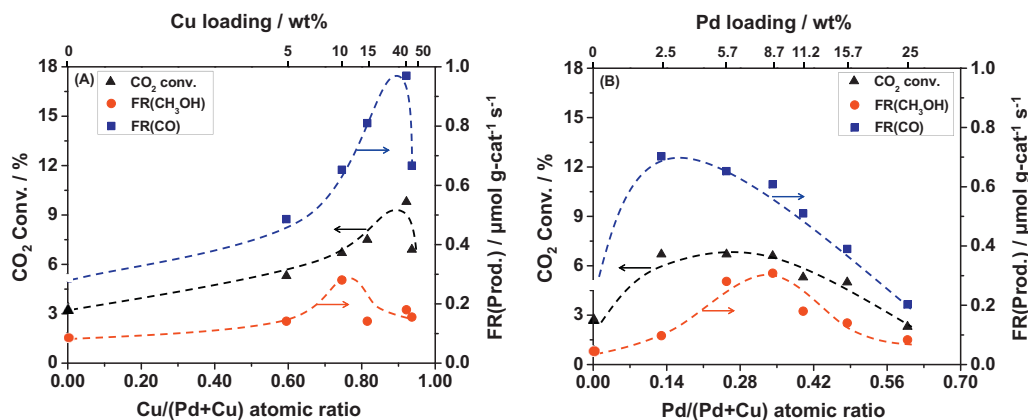


Fig. 1. Changes in CO₂ conversion and formation rate of products (CH₃OH and CO) over Pd–Cu(Y)/SiO₂ with fixed Pd loading at 5.7 wt% (A) and Pd(X)–Cu/SiO₂ with fixed Cu loading at 10 wt% (B) as functions of Cu/(Pd + Cu) and Pd/(Pd + Cu) atomic ratios, respectively. CO₂ hydrogenation: 523 K, 4.1 MPa, 6.2 g-cat h mol^{−1}.

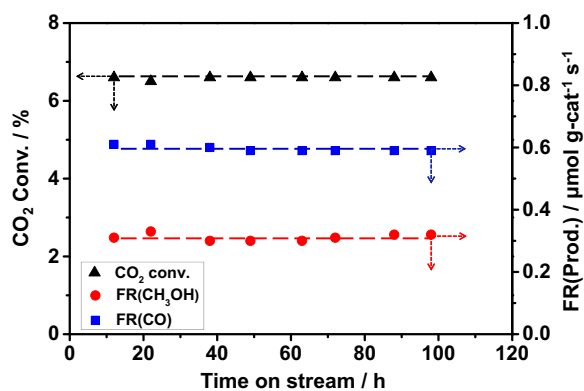


Fig. 2. Stabilities of CO₂ conversion and products formation rates with time on stream over Pd(0.34)-Cu/SiO₂ with Cu loading at 10 wt%. CO₂ hydrogenation: 523 K, 4.1 MPa, 6.2 g-cat h mol⁻¹.

sion and product formation rates remain constant during 100 h time on stream; no deactivation of the CH₃OH synthesis activity was observed.

3.1.2. Reaction pathways for methanol formation

In order to investigate the pathways for methanol formation, CO₂ hydrogenation was conducted using a Pd(0.34)-Cu/SiO₂ catalyst with flow velocities (W/F) ranging from 1.2 to 14.2 g-cat h mol⁻¹; the product selectivities were plotted as a function of CO₂ conversion in Fig. 3. CH₃OH selectivity is about 20 mol% at 1.5% CO₂ conversion. Afterwards, the selectivity of CH₃OH elevates gradually with the increase of CO₂ conversion, while the selectivity of CO changed in an opposite way. The initial selectivity of CH₃OH approaches to ca. 15 mol% by extrapolating the trend line of CH₃OH to zero conversion. Such significant selectivity to CH₃OH at zero conversion indicates that CO₂ is a primary carbon source for methanol synthesis over Pd-Cu bimetallic catalysts at lower CO₂ conversion. On the other hand, some of the byproduct CO, from reverse water-gas shift (RWGS), is likely to be converted to methanol at relatively higher CO₂ conversion, as CH₃OH selectivity increased and CO selectivity decreased in the mean time. This may also account for the observation that the formation rates for CH₃OH and CO maximize at different Pd/(Pd + Cu) ratios in Fig. 1B. Yang et al. [54] employed density functional theory (DFT) and kinetic Monte Carlo (KMC) simulations for examining

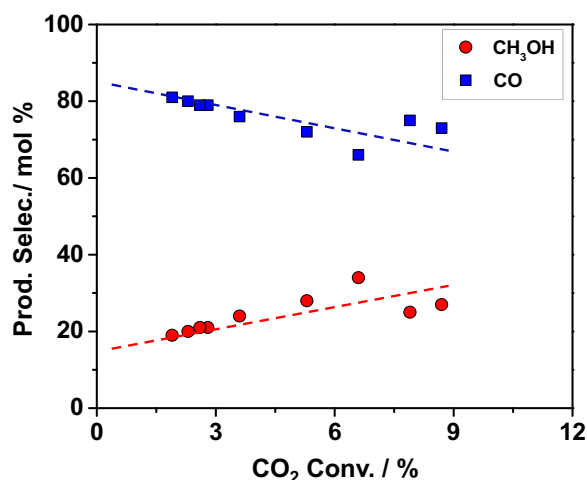


Fig. 3. Changes in products selectivity as a function of CO₂ conversion over Pd(0.34)-Cu/SiO₂ with Cu loading at 10 wt%. CO₂ hydrogenation: 523 K, 4.1 MPa, W/F = 1.2–14.2 g-cat h mol⁻¹.

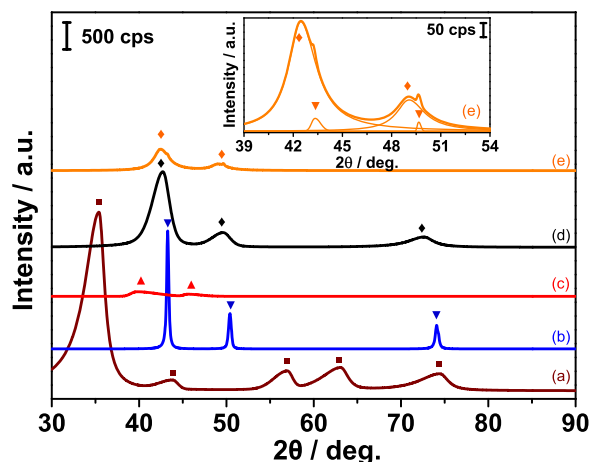


Fig. 4. XRD patterns of Pd(X)-Cu(Y)/SiO₂ catalysts with thick lines indicating original patterns and thin lines indicating deconvoluted patterns. (a) Calcined Pd(0.25)-Cu/SiO₂, (b) reduced Cu/SiO₂, (c) reduced Pd/SiO₂ with Pd loading at 5.7 wt%, (d) reduced Pd(0.25)-Cu/SiO₂, (e) reduced Pd(0.34)/Cu/SiO₂ with magnified pattern in the inset (2θ: 39–54°). Bimetallic catalyst samples were prepared by coimpregnation method, while sample (e) by sequential impregnation method. For all Cu containing samples, the Cu loading was 10 wt%. Symbols assignment: ▲: Pd⁰; ▼: Cu⁰; ◆: PdCu₃; ■: CuPdO₂.

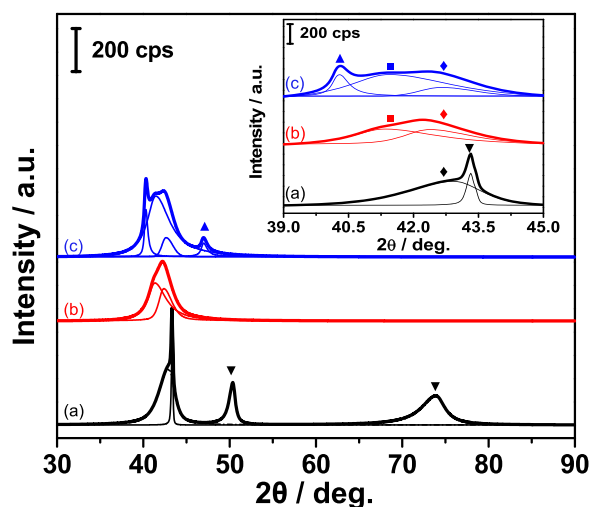


Fig. 5. XRD patterns of reduced Pd(X)-Cu/SiO₂ catalysts with magnified XRD patterns in the inset (2θ: 39–45°). (a) Pd(0.13)-Cu/SiO₂, (b) Pd(0.34)-Cu/SiO₂, (c) Pd(0.48)-Cu/SiO₂. Original patterns were highlighted with thick lines and patterns after deconvolution were featured with thin lines. For all samples, the Cu loading was 10 wt%. Symbols assignment: ▲: Pd⁰; ▼: Cu⁰; ◆: PdCu₃; ■: PdCu.

CH₃OH synthesis from CO₂ hydrogenation on Pd doped Cu₍₁₁₁₎ surface. They suggested that two reaction pathways were involved on Pd-Cu alloy surfaces: formate (intermediate) hydrogenation pathway and RWGS + CO hydrogenation pathway. Our experimental observations are in general agreement with their simulation results.

3.2. Support effect on CH₃OH formation over Pd-Cu bimetallic catalysts

Based on our previous work, we also examined the effect of different mesoporous supports on CH₃OH synthesis activity over Pd-Cu bimetallic catalysts, as summarized in Table 1. The Pd and Cu loadings were fixed at 5.7 wt% and 10 wt%, respectively, in order to compare with Ca-promoted Pd catalysts in our previous work [40]. The formation rate of CH₃OH over supported

Table 2
Physical properties of supported Pd(X)–Cu catalysts.^a

Catalyst ^b	BET surface area/m ² g-cat ⁻¹	Pore volume ^c /mL g-cat ⁻¹	Average pore ^d diameter/nm
Pd(0.13)–Cu/SiO ₂	304 (315)	0.9 (1.1)	9.9 (11.0)
Pd(0.25)–Cu/SiO ₂	305	0.9	9.4
Pd(0.34)–Cu/SiO ₂	309	0.8	9.3
Pd(0.48)–Cu/SiO ₂	292	0.8	8.9
Pd(0.25)–Cu/MCM-41	950 (1102)	1.1 (1.4)	3.6 (3.6)
Pd(0.25)–Cu/SBA-15	553 (719)	0.9 (1.2)	6.1 (6.3)
Pd(0.25)–Cu/MSU-F	457 (611)	1.6 (2.5)	12.0 (13.0)

^a Values in parentheses are for corresponding pristine support materials.

^b Cu loading was 10 wt% for all samples in the table.

^c BJH desorption cumulative pore volume.

^d BJH desorption average pore diameter.

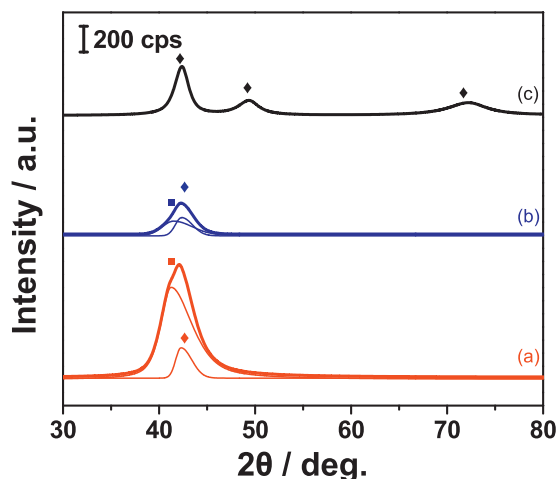


Fig. 6. XRD patterns of spent Pd(0.25)–Cu catalysts supported on (a) SBA-15, (b) MCM-41, (c) MSU-F. Original patterns were highlighted with thick lines, while thin lines were patterns after deconvolution. For all samples, the Cu loading was 10 wt%. Symbols assignment: \blacklozenge : PdCu₃; \blacksquare : PdCu.

Pd–Cu catalysts decreased in the following order: amorphous silica > SBA-15 ~ MCM-41 > MSU-F. The amorphous silica supported Pd–Cu catalyst showed the highest CH₃OH selectivity (31 mol%) among the bimetallic catalysts. It is also worth mentioning that the formation rates of CH₃OH over Pd–Cu catalysts supported on SBA-15, MCM-41 and MSU-F are greater than the sum of those over corresponding monometallic catalysts. Thus, bimetallic promotion on CH₃OH formation is observed for these supported Pd–Cu catalysts as well. XRD patterns (Figs. 5 and 6) confirm the alloy formation over bimetallic catalysts supported on these uniform mesoporous silicas, which is responsible for such significant synergistic effect on methanol promotion.

The effect of mesoporous silica supports on CH₃OH synthesis activity over a series of Ca-promoted Pd catalysts was studied in our early work [40]. The formation rate of CH₃OH varied with change of pore diameter of supports; the highest formation rate was obtained over Ca promoted Pd(5.7 wt%)/MCM-41, which yielded 0.22 $\mu\text{mol g-cat}^{-1} \text{s}^{-1}$ at 523 K and 4.1 MPa. In comparison, the bimetallic catalyst, Pd(0.25)–Cu/SiO₂ (Pd 5.7 wt%), improved the methanol formation rate by 27% at the same reaction condition.

3.3. Comparison to Cu–Zn based catalysts

Cu–Zn(Z)/SiO₂ catalysts were prepared similarly as Pd–Cu catalysts; their CO₂ hydrogenation activity and selectivity over a representative sample are shown in Table 1. The reaction was conducted at 523 K and 4.1 MPa, which is the same as Pd–Cu bimetallic catalysts. Cu loading was fixed at 10 wt%, and Zn/(Zn + Cu) atomic ratios were adjusted by changing Zn loading. Within the atomic

ratio range (ca. 0–0.80) tested, the CH₃OH formation rate was enhanced from 0.05 (Cu/SiO₂) to 0.12 $\mu\text{mol g-cat}^{-1} \text{s}^{-1}$ with gradually doping more Zn into Cu/SiO₂. However, the improvement is not as significant as Pd–Cu bimetallic catalysts, nor is the CO₂ conversion. Cu–Zn(0.67)/SiO₂ exhibited the maximum CH₃OH formation rate, 0.12 $\mu\text{mol g-cat}^{-1} \text{s}^{-1}$; however, it is not comparable to Pd(0.25)–Cu/SiO₂ catalyst with the same Cu loading (0.28 $\mu\text{mol g-cat}^{-1} \text{s}^{-1}$).

A commercial Cu–Zn–Al₂O₃ catalyst (MDC-3, Süd-Chemie, 40 wt% Cu) was also used for the CO₂ hydrogenation as reference. The results are compared in Table 1 as well. MDC-3 and Pd(0.25)–Cu/SiO₂ show similar product selectivity, whereas the formation rate of CH₃OH over Pd–Cu bimetallic catalyst is about 60% of that over MDC-3. In order to evaluate their metal efficiencies, the metal time yields were calculated by normalizing the CH₃OH formation rate to the total amount of metals in the catalyst. The metal time yields are 0.16 mmol mol-(Pd + Cu)⁻¹ s⁻¹ and 0.08 mmol mol-Cu⁻¹ s⁻¹ for Pd(0.25)–Cu/SiO₂ and MDC-3, respectively, implying that bimetallic Pd–Cu/SiO₂ exhibits better metal efficiency for CH₃OH formation than the MDC-3, even without considering the metal loading of Zn.

3.4. Physical properties of Pd–Cu catalysts

Physical properties of the calcined Pd–Cu bimetallic catalysts with different Pd/(Pd + Cu) atomic ratios are summarized in Table 2. Isotherms of all calcined catalysts are consistent with those of the support materials in the whole range of relative pressure (see Supplementary information, Fig. S3), implying that the mesopores are preserved in the calcined catalysts. The calcined Pd(X)–Cu/SiO₂ catalysts show decreasing values in surface area and pore volume in comparison to those of amorphous silica, especially in the cases of higher Pd/(Pd + Cu) atomic ratios. Such differences could be ascribed to impregnation of active metals. On the other hand, Table 2 also lists the physical properties of other structured-mesoporous silicas supported Pd–Cu catalysts together with those for corresponding pristine support materials. Both BET surface area and pore volume were reduced after metal loadings. Average pore diameters of the MSU-F and SBA-15 supported Pd(0.25)–Cu catalysts decreased by 1 nm and 0.2 nm, respectively; whereas such reduction is not seen in MCM-41 supported catalyst with smaller average pore diameters. The observed pore size reduction is attributed to the incorporation of Pd and Cu species into the mesopores of supports.

3.5. Crystallite structures of Pd–Cu catalysts

3.5.1. Amorphous silica supported Pd–Cu catalysts

The crystalline structures of calcined and reduced Pd(X)–Cu(Y)/SiO₂ catalysts were evaluated by X-ray diffraction measurements and resultant patterns are illustrated in

Table 3Crystallite phases, sizes and interplanar spacings for *reduced* Pd(X)–Cu/SiO₂ catalysts.

Catalyst ^a	Metal phase	$2\theta_{(111)}/^\circ$	Size ^b /nm	<i>d</i> -spacing ^c /nm
Cu	Cu ⁰	43.2	43	–
Pd(0.13)–Cu	PdCu ₃	42.7	5	0.21
	Cu ⁰	43.3	53	–
Pd(0.25)–Cu	PdCu ₃	42.6	4	0.21
	PdCu	41.4	4	0.22
Pd(0.34)–Cu	PdCu ₃	42.5	5	0.21
	Pd ⁰	40.5	23	–
Pd(0.48)–Cu	PdCu	41.5	3	0.22
	PdCu ₃	42.7	6	0.21
	Pd ⁰	40.5	3	–
Pd				

^a Cu loadings were fixed at 10 wt% for all Cu containing samples, and Pd loading was 5.7 wt% for Pd/SiO₂.

^b Crystallite size determined from Scherrer equation (Eq. (1)) for (1 1 1) peak.

^c Spacing between (1 1 1) planes in PdCu and PdCu₃ structure.

Figs. 4 and 5. The average crystallite sizes were determined by the Scherrer equation and summarized in Table 3.

In Fig. 4a, CuPdO₂ is observed for calcined Pd(0.25)–Cu/SiO₂ catalyst instead of separate oxides. Typical diffraction peaks of single metal phases (Cu⁰ and Pd⁰) are revealed in the XRD patterns of corresponding *reduced* monometallic Cu/SiO₂ (Fig. 4b) and Pd/SiO₂ (Fig. 4c) catalysts. Cu⁰ diffraction peaks are much sharper than Pd⁰, implying a larger Cu⁰ crystallite size compared to Pd⁰. This is confirmed by the estimated crystallite size based on Scherrer equation. The average crystallite size of Cu⁰ is 43 nm, which is considerably bigger than that of Pd⁰ (3 nm). This is indicative of a better dispersion for nano-sized Pd⁰ compared to Cu⁰. Interestingly, when Pd and Cu were combined together (see Fig. 4d), a major peak appears at $2\theta = 42.6^\circ$, which is centered between diffraction peaks for Pd₍₁₁₁₎ ($2\theta = 40.5^\circ$) and Cu₍₁₁₁₎ ($2\theta = 43.2^\circ$). Such a distinct peak could be assigned to the diffraction of alloy phase PdCu₃₍₁₁₁₎ with face-centered cubic (FCC) structure. Apart from PdCu₃₍₁₁₁₎ ($2\theta = 42.6^\circ$), additional diffractions appear at $2\theta = 49^\circ$ and 73° , corresponding to PdCu₃₍₂₀₀₎ and PdCu₃₍₂₂₀₎, respectively. This is in line with the observation by Hsieh and Whang [55] and Zhang et al. [56]. In addition, it is also worth mentioning that XRD pattern of the *spent* Pd(0.25)–Cu/SiO₂ catalyst shows an identical pattern as the fresh *reduced* Pd(0.25)–Cu/SiO₂ catalyst (not shown), demonstrating the preservation of PdCu₃ alloy phase during CO₂ hydrogenation.

In order to identify the impact of Pd loading on crystallite structure, three representative *reduced* Pd(X)–Cu/SiO₂ catalysts with different Pd/(Pd + Cu) ratios (ca. 0.13, 0.34, and 0.48) were examined by XRD. The resultant patterns are displayed in Fig. 5, together with an amplified inset showing the patterns after deconvolution. The crystallite structure information is summarized in Table 3. Fig. 5a shows the XRD of sample with Pd/(Pd + Cu) ratio at 0.13 (ca. 2.5 wt% Pd); multiple peaks overlap in the range between $2\theta = 40^\circ$ and 45° . After the deconvolution, it turns out to be the superposed diffractions of alloy phase PdCu₃₍₁₁₁₎ ($2\theta = 42.7^\circ$) and Cu⁰₍₁₁₁₎ ($2\theta = 43.3^\circ$). The other two diffractions in higher Bragg angles are typical peaks corresponding to Cu⁰₍₂₀₀₎ ($2\theta = 50^\circ$) and Cu⁰₍₂₂₀₎ ($2\theta = 74^\circ$). The crystallite sizes of PdCu₃ and Cu⁰ are estimated to be 5 nm and 53 nm, respectively. The large Cu⁰ crystallite size suggests the possibility of an agglomeration due to the excessive Cu loading under this composition. As illustrated in Fig. 5b, a dominant peak, centered at $2\theta = 42^\circ$, is present when the Pd/(Pd + Cu) ratio was increased to 0.34 (ca. 8.7 wt% Pd). After deconvolution, this superposed diffraction consists of peaks for alloy PdCu₃₍₁₁₁₎ ($2\theta = 42.5^\circ$) and alloy PdCu₍₁₁₁₎ ($2\theta = 41.4^\circ$) with body-centered cubic (BCC) structure; however, the Cu⁰ diffractions diminish. The estimated average crystallite sizes of PdCu and PdCu₃ are 4 nm and 5 nm, respectively. The absence of the Cu⁰ peak indicates that the formation of Pd–Cu alloy phases improves Cu dispersion. Fig. 5c illustrates the XRD pattern

of the catalyst with a greater Pd/(Pd + Cu) atomic ratio of 0.48 (ca. 15.7 wt% Pd). From the inset Fig. 5c, three different phases coexist: Pd⁰ ($2\theta = 40.5^\circ$), alloy PdCu ($2\theta = 41.5^\circ$) and alloy PdCu₃ ($2\theta = 42.7^\circ$), with crystallite sizes of 23 nm, 3 nm, and 6 nm, respectively. It is apparent that higher Pd/(Pd + Cu) atomic ratio of Pd–Cu catalyst leads to the agglomeration of Pd⁰ particles as evidenced by the larger crystallite size of Pd⁰ than those of alloy Pd–Cu particles.

In addition, the *reduced* catalyst prepared by sequential impregnation, Pd(0.34)/Cu/SiO₂, was also examined by XRD, as shown in Fig. 4e along with an amplified inset showing the region with multiple diffractions. Interestingly, unlike the coimpregnated sample with the same metal loadings (Fig. 5b), sequentially prepared Pd/Cu/SiO₂ shows PdCu₃ alloy ($2\theta = 42.6^\circ$) and Cu⁰ diffraction (ca. $2\theta = 43.2^\circ$) instead of PdCu₃ and PdCu alloy phases. Similar results were observed for *reduced* Cu/Pd/SiO₂ prepared by reverse order (see Supplementary information, Fig. S4). It should be noted that the sequentially impregnated samples were prepared without intermediate calcination, which would preserve the first impregnated metal salt in the second step. Therefore, it provides an opportunity for at least part of the first impregnated metal salt to redissolve and thus mix with second metal salt in solution. This is evidenced by the color variation during second impregnation. The precursor solution changes from its original color (orange for Pd acetate and blue for Cu nitrate) to green during the second impregnation, which is characteristic when dissolving Pd and Cu salts together. However, such partial redissolution is inadequate for mixing Pd and Cu in the solution compared to coimpregnation, resulting in the presence of PdCu₃ and absence of PdCu. Besides, the similar tendency to greenish solution during the second impregnation would suggest identical chemical states of metal salts regardless of preparation order, and one would expect the same crystallite structures as observed from XRD patterns. On the other hand, the variation of alloy phases between coimpregnated and sequentially impregnated samples indicates the significance of preparation method on Pd–Cu alloy formation. In other words, the coimpregnation method favors formation of alloy phases by forming homogeneous solution.

3.5.2. Effect of support on Pd–Cu alloy formation

The effect of support on Pd–Cu alloy formation was evaluated by XRD over *spent* Pd–Cu catalysts, as illustrated in Fig. 6 where the Pd/(Pd + Cu) atomic ratio was kept constant at 0.25 (Cu 10 wt%). In Fig. 6a and b, major peaks, centered at $2\theta = 42^\circ$, are observed in the cases of SBA-15 and MCM-41 supported bimetallic catalysts. Deconvolution over these superposed diffractions show the coexistence of two alloy phases PdCu and PdCu₃, which disagrees with the observation of single alloy (PdCu₃) in the amorphous silica supported catalyst with the same composition (see Fig. 4d). However, MSU-F supported Pd–Cu catalyst (Fig. 6c) explicitly reveals identical alloy phase PdCu₃ as amorphous silica supported sample. These results suggest that 2D pore structures with smaller pore sizes and/or surface chemical natures of MCM-41 and SBA-15 have crucial impact on the Pd–Cu alloy formation. Nevertheless, the estimated crystallite sizes of PdCu and PdCu₃ in these supported catalysts are quite similar to amorphous silica supported one, ranging from 3 to 6 nm.

3.6. Morphological properties of Pd and Cu species

Fig. 7 shows typical TEM images of a *reduced* Pd(0.34)–Cu/SiO₂ catalyst, which have both PdCu and PdCu₃ alloy phases in reduced form as mentioned in Section 3.5.1. As illustrated from Fig. 7A and B, the particles are widely dispersed over the support. Fig. 7C is an image of this sample with high resolution and the lattice fringes align clearly parallel to each other. The lattice space is measured to be ~ 0.20 nm on average, which matches the value of the *d*-spacing of Pd–Cu alloys estimated from XRD results (see Table 3).

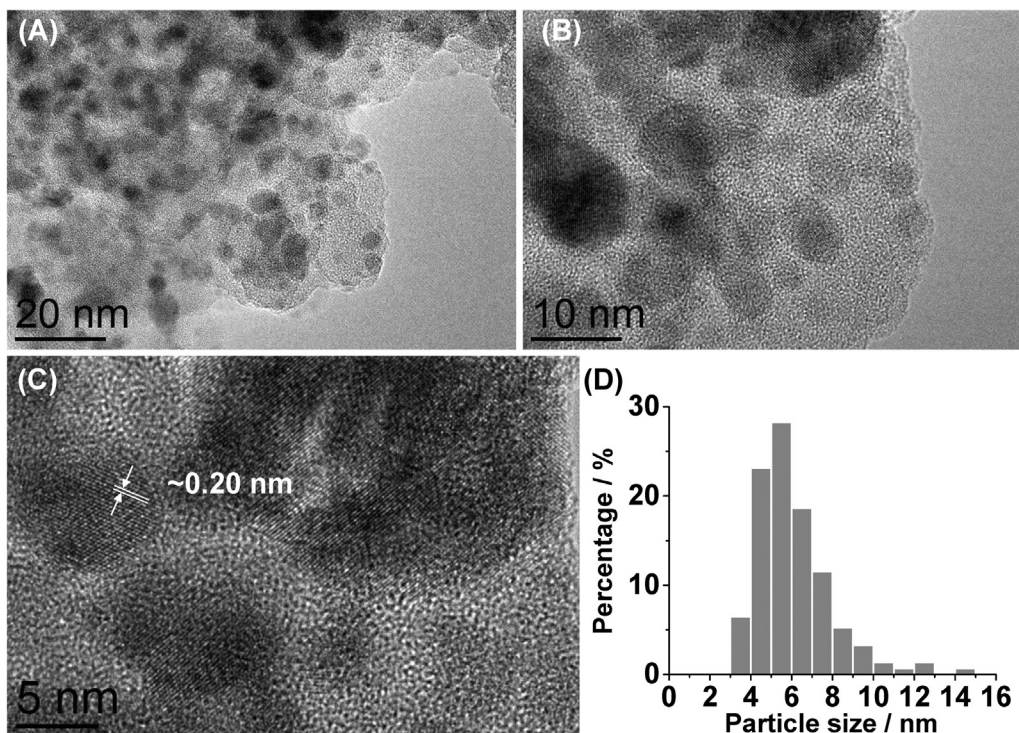


Fig. 7. TEM images of *reduced* Pd(0.34)–Cu/SiO₂ (Cu = 10 wt%) with different magnifications (A–C). The lattice fringe pattern of ca. 0.2 nm is discernible in image (B). (D) represents the corresponding particle size distribution.

Approximate 150 particles were chosen to estimate the particle size distribution and results are shown in Fig. 7D. The average particle size primarily lies in the range of 4–7 nm, which coincides with XRD results (4–5 nm, Table 3). Therefore, it is suggested that these nano-sized particles represent the Pd–Cu alloy particles. However, the lattice space is quite similar among alloy particles, which makes it hard to distinguish PdCu from PdCu₃.

The presence of Pd–Cu alloy particles was also evidenced by Z-contrast in the high-angle annular dark-field image (HAADF) of *reduced* Pd(0.34)–Cu/SiO₂ in Fig. 8A. All particles are nano-sized and well-dispersed. The magnified inset shows a representative particle with relatively clear lattice fringe alignment. The average *d*-spacing is about 0.21 nm on average, which matches the results from TEM images and XRD patterns. Therefore, these particles are representative alloy particles. In order to further confirm the alloy formation, the same area in the HAADF image was scanned by energy-dispersive X-ray spectroscopy mapping technique in STEM mode (STEM/EDS). This cutting-edge technique allows us to identify the elemental compositions of individual bimetallic nanoparticles on the surface of silica support. It is worth noting that a carbon-coated molybdenum grid was applied, instead of copper grid, to improve accuracy in both mapping and quantifying Cu and Pd species. The EDS mappings reveal that Si and O species distribute uniformly across the sample island (see Supplementary Fig. S5), while Pd and Cu species exist in close proximity but at different relative concentrations.

In order to unveil the relation between Pd and Cu species, overlapping EDS maps were generated subsequently including two-element (Fig. 8B) and four-element maps (see Supplementary information, Fig. S6). Interestingly, the distributions of Pd and Cu species coincide perfectly with each other in location. When comparing those Pd–Cu clusters (circled by boxes) with corresponding particles in HAADF image (Fig. 8A), it is apparent that Pd and Cu distribute homogeneously within the bimetallic particles, and thus these are Pd–Cu alloy particles. On the other hand, those circled particles, which are distinct in shape in HAADF image, were

Table 4

Quantified phase compositions in the alloyed Pd–Cu nanoparticles from STEM/EDS maps.^a

Particle #	Analyzed composition/at.% ^b		Cu/Pd ratio/at. at. ^{-1c}
	Cu-K	Pd-L	
1	23.22	15.91	PdCu _{1.5}
2	16.37	9.24	PdCu _{1.8}
3	11.03	4.14	PdCu _{2.7}
4	3.93	3.77	PdCu _{1.0}
5	29.10	34.89	PdCu _{0.8}
6	5.68	4.23	PdCu _{1.3}
7	8.57	3.01	PdCu _{2.8}
8	13.10	15.42	PdCu _{0.8}
9	4.96	6.57	PdCu _{0.8}

^a Sample: *reduced* Pd(0.34)–Cu/SiO₂, with Cu loading at 10 wt%.

^b Uncertainty of each element in quantitative analysis: O (1.11 at%); Si (0.60 at%); Cu (0.31 at%); Pd (0.38 at%).

^c Values in subscript were ratios of Cu/Pd with the unit of at. at.⁻¹.

chosen for quantification and the composition is listed in Table 4. The Cu/Pd ratios are in the range of 1.0–3.0, which confirms the coexistence of alloy phases PdCu and PdCu₃. Therefore, these observations demonstrate homogeneous distribution of PdCu and PdCu₃ alloys on the *reduced* catalyst and strongly support XRD results over the same sample (Fig. 5b).

Fig. 9 shows typical TEM images of *reduced* Pd(0.25)–Cu/SBA-15 catalyst, for which both of the two Pd–Cu alloy phases were observed from XRD pattern (Fig. 6a). Fig. 9A reveals a representative image of 2D channels of SBA-15. Fig. 9B and C exhibit an interesting dispersion of Pd–Cu alloy particles which align along with the 2D channels. The reason for this homogeneous and regular dispersion of Pd–Cu alloy particles can be attributed to the unique pore structure of SBA-15. Fig. 9D illustrates the distribution of particles sizes, which were derived by measuring about 150 particles. Particle sizes distribute primarily in the range of 5–8 nm, which is reasonable as compared to the average value estimated from XRD (~6 nm).

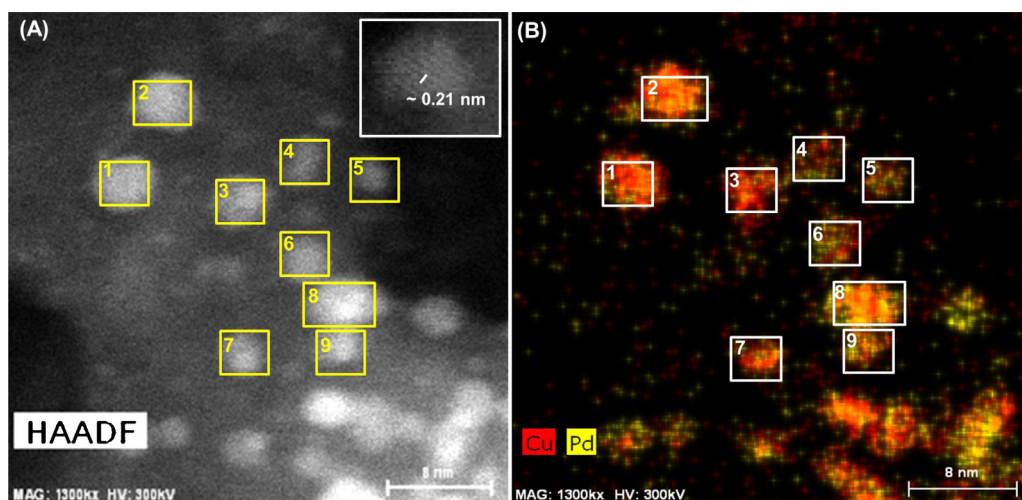


Fig. 8. (A) HAADF STEM image of *reduced* Pd(0.34)–Cu/SiO₂ (Cu = 10 wt%) with a representative alloy particle in the inset and corresponding STEM/EDS overlap maps for Pd and Cu (B). A representative alloy particle was magnified in the inset showing clear fringe alignment.

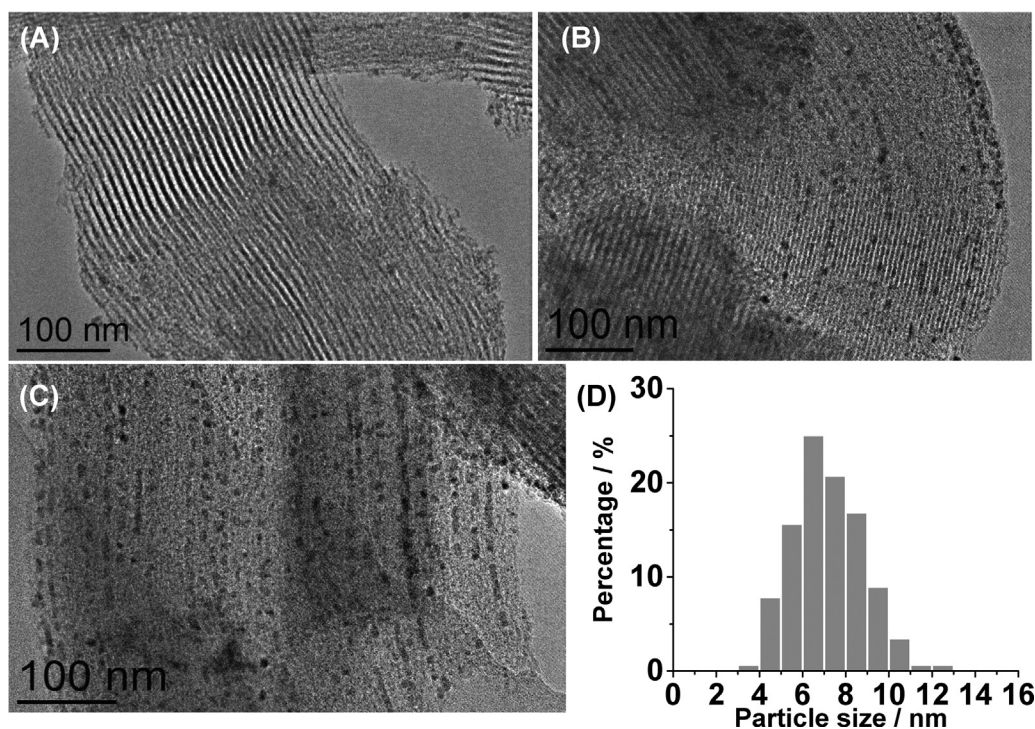


Fig. 9. TEM image (A) shows the characteristic pore structure of SBA-15. (B and C) are TEM images of *reduced* Pd(0.25)–Cu/SBA-15 (Cu = 10 wt%) with different areas. (D) represents the corresponding particle size distribution.

3.7. Surface properties of *reduced* Pd–Cu catalysts

To investigate the surface chemical nature of Pd and Cu, Fig. 10 depicts the XPS spectra in the Pd 3d region for Pd/SiO₂ and Pd(0.34)–Cu/SiO₂; the corresponding XPS data are summarized in Table 5. The *reduced* Pd/SiO₂ exhibits an intense doublet centering at 335.1 and 340.4 eV, assigned to Pd 3d_{5/2} and Pd 3d_{3/2}, respectively, with a spin–orbit coupling energy of 5.3 eV. The observed BEs closely match with Pd metal in Table 5, which implies the existence of metallic state (Pd⁰). However, a fraction of Pd oxide may be contained as the peaks are slightly asymmetric. The doublet for *reduced* Pd(0.34)–Cu/SiO₂ catalyst appears with similar BEs. In a previous study [57], Pd 3d doublet of bulky Pd–Cu alloy did not show apparent peak shift with respect to the pure metal. Venezia et al. [58]

observed identical result over pumice supported Pd–Cu sample in reduced state as compared to monometallic catalyst. Therefore, Pd⁰ is suggested to be the primary state in the bimetallic catalyst. On the other hand, intensities of doublet decrease in bimetallic sample. Such reduction is due to a decreased surface concentration of Pd in the alloy compared to pure Pd.

The Cu 2p core level XP spectra for *reduced* Cu/SiO₂ and *reduced* Pd(0.34)–Cu/SiO₂ are shown in Fig. 11; the XPS data are gathered in Table 6. Cu/SiO₂ exhibits a linear superposition of distinct spectra in the typical BE ranges of both Cu 2p_{3/2} and 2p_{1/2}. Considering the relevant BEs of copper oxides, copper metal, and copper in alloys in Table 6, the spectrum primarily contains two components, one due to Cu metal as a sharp and intense peak at 931.9 eV and the other to CuO which is a shoulder peak around 934 eV and shake-up

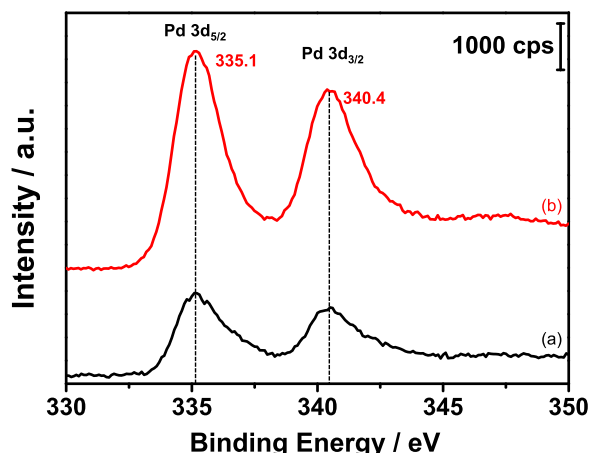


Fig. 10. Pd 3d XP spectra of (a) reduced Pd(0.34)-Cu/SiO₂; (b) reduced Pd/SiO₂. Pd loading was 8.7 wt% for two samples.

Table 5
Pd 3d XPS parameters of reduced Pd-Cu/SiO₂ catalysts.

Catalyst	Pd 3d _{5/2} BE/eV	Pd 3d _{3/2} BE/eV	ΔE/eV
Pd ^a	335.1	340.4	5.3
Pd(0.34)-Cu ^a	335.2	341.6	5.4
Pd-Cu/pumice ^b	334.8	–	–
Pd-Cu/CeO ₂ ^c	335.3	340.3	5.0
PdO ^d	336.3	–	–
PdO ₂ ^e	337.9	–	–
Pd metal ^d	335.0	–	–

^a Pd loading was 8.7 wt% for two samples.

^b Data was acquired by in situ method over reduced sample, see Ref. [58].

^c Data was acquired by “pseudo in situ” method over reduced sample, see Ref. [59].

^d Ref. [60,61].

^e Ref. [62].

satellites above the main photoelectron transition. Such assignment can be applied to the spectrum of reduced Pd(0.34)-Cu/SiO₂ as well. Venezia et al. [58] acquired XPS data by in situ method over reduced sample and found that the Cu 2p peaks of Pd-Cu catalyst shifted about 0.5 eV below the BE of monometallic Cu sample as a result of Pd-Cu alloy formation. An alloy-induced negative peak shift (~0.4 eV) was reported in a previous work by “pseudo in situ” method [59]. However, such a shift was not observed in this work. Recalling that our samples were slowly passivated after

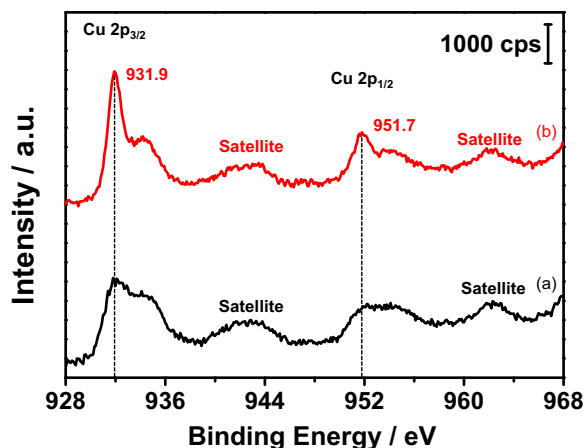


Fig. 11. Cu 2p XP spectra of (a) reduced Pd(0.34)-Cu/SiO₂; (b) reduced Cu/SiO₂. Cu loading was 10 wt% for two samples.

Table 6
Cu 2p XPS parameters of reduced Pd-Cu/SiO₂ catalysts.

Catalyst	Cu 2p _{3/2} BE/eV	Cu 2p _{1/2} BE/eV	ΔE/eV
Cu ^a	931.9	951.7	19.8
Pd(0.34)-Cu ^a	932.0	951.8	19.8
Pd-Cu/pumice ^b	931.9	–	–
PdCu/CeO ₂ ^c	932.0	951.6	19.6
CuO ^d	934.6	–	–
Cu ₂ O ^d	932.8	–	–
Cu metal ^d	932.8	–	–

^a Cu loading was 10 wt% for two catalysts.

^b Data was acquired by in situ method over reduced sample, see Ref. [58].

^c Data was acquired by “pseudo in situ” method over reduced sample, see Ref. [59].

^d Ref. [63].

reduction, accordingly the photoelectron from CuO was inevitable, which hinders us from confirming the subtle peak shift. Nevertheless, the intensity of that distinct peak for reduced Cu/SiO₂, centered at 931.9 eV, decreased dramatically in reduced bimetallic sample, suggesting the detection of more copper oxides over the surface. In a previous work [59], Pd EXAFS showed the evidence of Pd-Cu alloy formation and Pd had about 4Cu neighbors, which lowered the surface concentration of Pd. Moreover, considering the facts that Cu particle size decreases dramatically with the alloy formation (Table 3) and distributions of Pd and Cu coincide well with each other in location as observed from EDS map (see Fig. 8), the intimacy between Pd and Cu is critical in improving the dispersion of Cu over the surface to form fine particles. These Cu-containing fine particles are more easily oxidized compared to larger monometallic Cu particles. Therefore, more surface oxide is expected as well as the decreasing intensity of Cu 2p_{3/2} peak. The estimated surface composition based on XPS is presented in Table 7. It is apparent that the Cu concentration increased in bimetallic catalyst due to the formation of smaller alloy particles over the surface, and Pd concentration lowers because of intimate interaction with surrounding Cu. The observed results indicate the existence of a strong interaction between these Pd and Cu metals in reduced bimetallic sample.

3.8. H₂ adsorption properties of Pd-Cu catalysts

Fig. 12 presents H₂-TPD profiles over monometallic and bimetallic catalysts. Prior to TPD, all samples were reduced in situ at 573 K for 2 h. For the monometallic catalysts, Cu/SiO₂ hardly shows desorption peaks (Fig. 12a); while Pd/SiO₂ shows multiple peaks in the whole temperature range (Fig. 12b). It is suggested that Cu/SiO₂ catalyst has a negligible H₂ chemisorption capacity, or hydrogen atoms adsorb on the Cu⁰ surface so weakly that they are removed easily during He flushing prior to TPD. In contrast, TPD profile of Pd/SiO₂ catalyst reflects its strong hydrogen chemisorption capacity.

To identify the hydrogen adsorption properties of Pd-Cu bimetallic catalysts, Pd(X)-Cu/SiO₂ catalysts (ca. Cu 10 wt%) were evaluated by H₂-TPD, and representative profiles are compared in

Table 7
Surface chemical compositions of reduced Pd-Cu/SiO₂ catalysts determined by XPS.^a

Catalyst	Composition/at%				
	Cu	Pd	Si	C	O
Cu/SiO ₂	0.63	–	31.97	3.09	64.31
Pd/SiO ₂	–	1.12	31.06	2.63	65.19
Pd(0.34)-Cu/SiO ₂	0.92	0.44	31.22	3.27	64.15
SiO ₂	–	–	32.31	2.84	64.85

^a Cu loading was 10 wt% for Cu containing samples while Pd loading was 8.7 wt% for Pd containing samples.

Table 8Amount of H₂ desorbed during H₂-TPD of reduced Pd(X)–Cu/SiO₂ catalysts.^{a,b,c}

Catalyst	Amount of desorbed H ₂ /μmol g-cat ⁻¹		Percentage of H ₂ desorbed below 500 K/%
	Total	Below 500 K ^d	
Cu	1.1	0.2	18
Pd(0.13)–Cu	2.4 (7.0)	0.6 (1.7)	25 (24)
Pd(0.25)–Cu	15.3 (37.4)	6.3 (6.9)	41 (18)
Pd(0.34)–Cu	23.9 (37.9)	16.6 (7.6)	69 (20)
Pd(0.48)–Cu	32.0 (56.5)	10.0 (9.7)	31 (17)

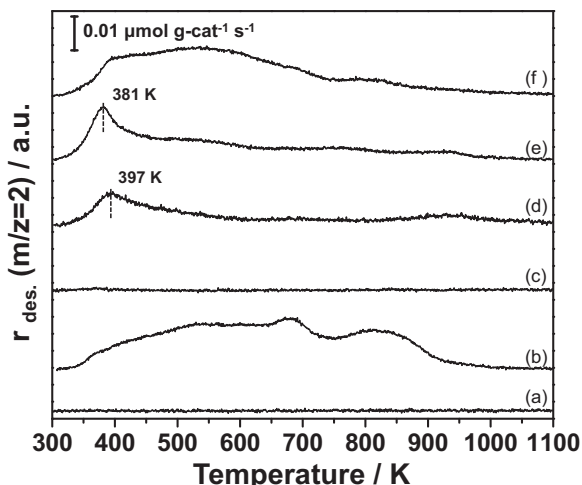
^a TPD condition: 1 vol% Ar/He (30 mL min⁻¹), 10 K min⁻¹ of heating rate.^b For Cu containing samples, the Cu loading was 10 wt%.^c All values in the parentheses were estimated based on H₂-TPD profiles of reduced monometallic Pd/SiO₂ catalysts with the same Pd loadings as corresponding bimetallic catalysts.^d Amount of H₂ desorbed below 500 K.**Fig. 12.** H₂-TPD profiles of reduced catalysts. (a) Cu/SiO₂, (b) Pd/SiO₂ with Pd loading at 8.7 wt%, (c) Pd(0.13)–Cu/SiO₂, (d) Pd(0.25)–Cu/SiO₂, (e) Pd(0.34)–Cu/SiO₂, (f) Pd(0.48)–Cu/SiO₂. For all Cu containing samples, the Cu loading was 10 wt%.

Fig. 12c–f. Fig. 12c shows the TPD profile over the bimetallic catalyst with Pd/(Pd + Cu) atomic ratio as low as 0.13 (ca. Pd 2.5 wt%); the hydrogen desorption curve is quite similar to that for monometallic Cu catalyst. This is indicative of a Cu⁰-dominant surface. Considering the presence of PdCu₃ and Cu⁰ phases for exactly the same sample in XRD pattern (see Fig. 5a), it is suggested that the PdCu₃ particle is partially covered by the Cu⁰ layer. Fig. 12d and e exhibit the TPD profiles of the bimetallic samples with Pd/(Pd + Cu) ratios at 0.25 (ca. Pd 5.7 wt%) and 0.34 (ca. Pd 8.7 wt%), respectively; a distinct hydrogen desorption peak, centered at 380–400 K, appears. That the hydrogen desorption peaks occur at lower temperature (300–500 K) is an interesting observation that implies the existence of weakly-bonded hydrogen atoms over the surface. Fig. 12f depicts the TPD profile of a Pd-rich bimetallic sample with Pd/(Pd + Cu) ratio at 0.48 (ca. Pd 15.7 wt%). The desorption profile is similar to that for monometallic Pd catalyst in the whole temperature range. This demonstrates the surface is dominated primarily by Pd⁰ due to excessive loading. Recalling that this sample contains Pd⁰ with large particles, apart from PdCu₃ and PdCu (Fig. 5c), it is suggested that Pd–Cu alloy particle is partially covered by Pd⁰ layer.

Hydrogen adsorption capacity was also evaluated by quantitative analysis of TPD profiles. The desorbed hydrogen amount was estimated by integration, as summarized in Table 8. Generally, the total amount of hydrogen desorbed from Pd(X)–Cu/SiO₂ catalysts enhances monotonically with the increase of Pd/(Pd + Cu) ratio from 0.13 to 0.48. In contrast, within the same atomic ratio range, the amount of weakly-bonded hydrogen (<500 K) increases initially and then decreases after reaching a maximum value at 0.34, where the weakly-bonded hydrogen (<500 K) accounts for

about 70% of the total desorbed hydrogen. Moreover, this sample, Pd(0.34)–Cu/SiO₂, also exhibits significant advantage in both desorbed amount and proportion of weakly-bonded hydrogen (<500 K) compared to corresponding monometallic Pd/SiO₂.

Considering the significant impact of Pd/(Pd + Cu) ratios on the formation of alloy phases (Section 3.5.1), it is suggested that Pd–Cu alloy formation affects H₂ adsorption property, because the H₂-TPD profiles varies with Pd/(Pd + Cu) ratios. Excessive loading of one metal could cause partial coverage of alloy particles, and thus exhibiting similar TPD profile as corresponding monometallic catalyst. On the other hand, appropriate composition would lead to the formation of alloys, and therefore exhibiting characteristic desorption properties different from monometallic catalysts, especially below 500 K. Among these catalysts, Pd(0.34)–Cu/SiO₂ shows considerable advantage in the desorbed amount of weakly-bonded hydrogen (<500 K). Based on XRD and STEM/EDS results for this sample, it is suggested that such advantage is due to the well-dispersed PdCu and PdCu₃ alloy particles. In other words, the coexistence of well-dispersed alloys (PdCu and PdCu₃) would provide a source of chemisorbed hydrogen atoms, which is a promising property to benefit CH₃OH formation from CO₂ hydrogenation.

3.9. Importance of Pd–Cu alloy formation for bimetallic promotion

As discussed in Section 3.1, notable bimetallic promotion of CH₃OH formation appears over supported Pd(0.25)–Cu bimetallic catalysts. Characterization results demonstrate the formation of Pd–Cu alloys is dependent on Pd/(Pd + Cu) ratio, and thereby affect hydrogen adsorption capacity. In order to identify the relationship between Pd–Cu alloy formation and bimetallic promotion of CH₃OH synthesis, the extent of “CH₃OH promotion” was defined as a ratio of CH₃OH formation rate over bimetallic catalyst (numerator) to the summation of CH₃OH formation rates over corresponding monometallic catalysts (denominator), as shown in Eq. (2).

$$\text{CH}_3\text{OH promotion} = \frac{\text{FR}(\text{CH}_3\text{OH})_{\text{Pd-Cu}}}{\text{FR}(\text{CH}_3\text{OH})_{\text{Pd}} + \text{FR}(\text{CH}_3\text{OH})_{\text{Cu}}} \quad (2)$$

Fig. 13A shows the CH₃OH promotion level plotted as a function of Pd/(Pd + Cu) atomic ratio. Similar to CH₃OH formation rate, CH₃OH promotion level exhibits volcano-like curve in the whole range of Pd/(Pd + Cu) atomic ratio and maximizes at 0.34 (ca. Pd 8.7 wt%). Based on characterization results, this catalyst, Pd(0.34)–Cu/SiO₂, forms two well-dispersed Pd–Cu alloy phases after reduction at 573 K, namely PdCu and PdCu₃. However, other bimetallic catalysts contain either one alloy phase (ca. atomic ratio = 0.25) or single metallic phase (ca. atomic ratio = 0.13 or 0.48). Moreover, Pd(0.34)–Cu/SiO₂ adsorbs more weakly-bonded hydrogen at lower temperature (<500 K) in comparison to other

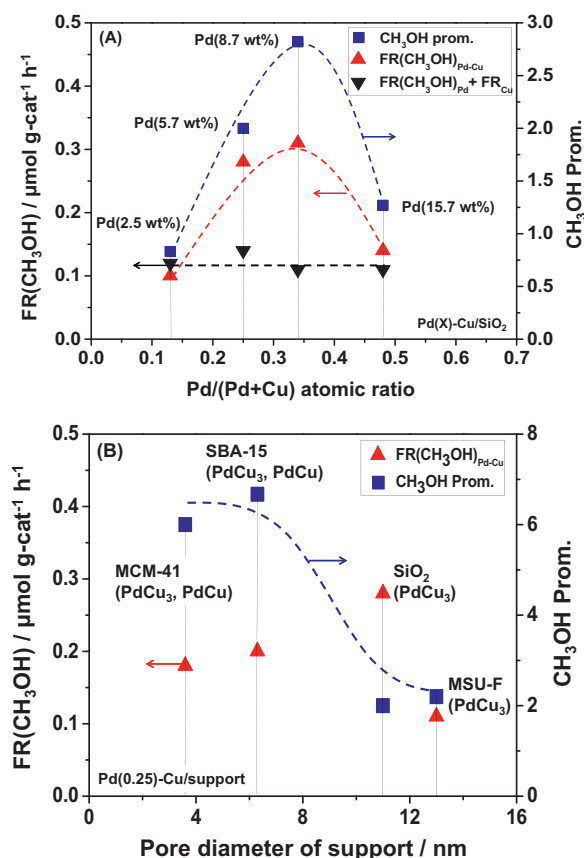


Fig. 13. Bimetallic promotion of CH₃OH formation over (A) amorphous silica-supported Pd(X)-Cu/SiO₂ and (B) uniform mesoporous silica-supported Pd(0.25)-Cu catalysts. Cu loadings for all samples were 10 wt%.

bimetallic catalysts. The presence of Pd–Cu alloys is responsible for the methanol promotion over Pd(X)-Cu/SiO₂ catalysts, particularly in the condition of coexisted PdCu and PdCu₃ without unalloyed metals.

For Cu–Zn based catalysts, the mechanism of methanol synthesis has been proposed to proceed via CO₂ conversion to surface formate species which is then hydrogenated to methoxide and ultimately to methanol [64]. Fujitani and Nakamura [27] reported that the Cu–Zn alloy promoted the hydrogenation of formate species to methoxide, a postulated rate determining step. Similarly, it is suggested that the formation of Pd–Cu alloy could also benefit the chemisorption of CO₂ and hydrogenation of the adsorbed intermediate species by providing more weakly-bonded hydrogen over the alloy surface, and thus leading to pronounced CH₃OH promotion. However, this is the area where more in-depth study is needed in future.

The significance of Pd–Cu alloy phases could also be considered as an important factor for the lower activity of sequentially impregnated samples compared to coimpregnated one. Unlike coimpregnated sample Pd(0.34)-Cu, the sequentially loaded catalysts (Pd/Cu and Cu/Pd) show PdCu₃ alloy alone and along with Cu⁰ regardless of impregnation sequence (Fig. 4 and S4). As discussed in Section 3.5.1, such variation can be attributed to the effect of preparation method. In other words, compared to sequential impregnation, coimpregnation method assists the alloy formation by mean of forming homogeneous precursor solution and thereby benefit CH₃OH promotion.

CH₃OH promotion level was also plotted for Pd–Cu bimetallic catalysts on uniform mesoporous silicas as a function of pore diameter of supports in Fig. 13B. Apparently, MCM-41 and SBA-

15 supported Pd–Cu catalysts with two alloy phases (PdCu₃ and PdCu) show stronger promotional effect on CH₃OH than other catalysts with single alloy phase. As suggested in Section 3.5.2, the special features of MCM-41 and SBA-15, unique 2D pore structure with relatively smaller pore diameter and/or surface chemical nature, may play an important role in the formation of two well-mixed alloyed phases, therefore, resulting in a better performance on CH₃OH promotion.

4. Conclusions

In the present work, Pd–Cu bimetallic catalysts were prepared and studied in the CO₂ hydrogenation for methanol synthesis. The effects of Pd–Cu composition and types of SiO₂ supports were also examined. Important results are summarized below.

- (1) The combination of Cu and Pd led to a strong synergistic promotion of CH₃OH formation rate when the Pd/(Pd + Cu) atomic ratios were within 0.25–0.34 for amorphous silica supported Pd–Cu catalysts. Similar promotional effects were observed over other catalysts loaded on uniform mesoporous silica such as SBA-15, MCM-41, and MSU-F.
- (2) Pd(0.34)-Cu/SiO₂ showed the maximum CH₃OH formation rate among all bimetallic catalysts tested. Its catalytic activity was stable and no apparent deactivation was observed over 100 h on stream.
- (3) XRD results demonstrate that the formation of Pd–Cu alloy is affected by Pd/(Pd + Cu) ratio. Nano-sized alloy particles were observed from high-resolution TEM images. STEM/EDS maps revealed the elemental compositions of individual Pd–Cu nanoparticles on support surface and confirmed the existence of PdCu and PdCu₃ alloy phases from quantitative analysis. XPS data confirmed the strong interaction between Pd and Cu due to the alloy formation. The H₂-TPD results provide an insight into the role of the alloy formation in the adsorption states of hydrogen.
- (4) Based on the formation of Pd–Cu alloy phases and their impact on CH₃OH promotion, Pd–Cu alloy formation is suggested to be a crucial factor for the bimetallic promotion, particularly in the coexistence of PdCu and PdCu₃ alloy phases without unalloyed metallic phases.
- (5) In the range of CO₂ conversion studied, CO₂ appears to be a primary carbon source for methanol formation over Pd–Cu/SiO₂ catalysts at lower CO₂ conversion; while byproduct CO contributes also to methanol synthesis through CO hydrogenation at higher CO₂ conversion.

Acknowledgements

This work was supported in part by the Pennsylvania State University through the Penn State Institute of Energy and the Environment. The STEM/EDS and XPS were performed at the Materials Characterization Laboratory of the Penn State Materials Research Institute, for which the assistance of Jennifer Gray and Vincent Bojan is gratefully acknowledged. One of the authors (XJ) acknowledges the financial support from Chinese Scholarship Council (CSC).

Appendix A. Supplementary data

Supplementary data associated with this article can be found, in the online version, at <http://dx.doi.org/10.1016/j.apcatb.2015.01.010>.

References

- [1] M.B. Ansari, S.-E. Park, *Energy Environ. Sci.* 5 (2012) 9419–9437.
- [2] R.W. Dorner, D.R. Hardy, F.W. Williams, H.D. Willauer, *Energy Environ. Sci.* 3 (2010) 884–890.
- [3] P. Markewitz, W. Kuckshinrichs, W. Leitner, J. Linssen, P. Zapp, R. Bongartz, A. Schreiber, T.E. Muller, *Energy Environ. Sci.* 5 (2012) 7281–7305.
- [4] W. Wang, S. Wang, X. Ma, J. Gong, *Chem. Soc. Rev.* 40 (2011) 3703–3727.
- [5] Z. Jiang, T. Xiao, V.L. Kuznetsov, P.P. Edwards, *Philos. Trans. R. Soc. A* 368 (2010) 3343–3364.
- [6] C. Song, in: C. Song, A.F. Gaffney, K. Fujimoto (Eds.), *CO₂ Conversion and Utilization*, American Chemical Society, Washington DC, 2002, pp. 2–30.
- [7] C. Song, *Catal. Today* 115 (2006) 2–32.
- [8] M. Mikkelsen, M. Jorgensen, F.C. Krebs, *Energy Environ. Sci.* 3 (2010) 43–81.
- [9] H. Arakawa, M. Aresta, et al., *Chem. Rev.* 101 (2001) 953–996.
- [10] M. Aresta, A. Dibenedetto, *Catal. Today* 98 (2004) 455–462.
- [11] M. Aresta, in: M. Aresta (Ed.), *Carbon Dioxide as Chemical Feedstock*, Wiley-VCH Verlag GmbH & Co. KGaA, Weinheim, 2010, pp. 1–13.
- [12] G. Centi, S. Perathoner, Z.S. Rak, *Appl. Catal. B* 41 (2003) 143–155.
- [13] G. Centi, S. Perathoner, *Catal. Today* 148 (2009) 191–205.
- [14] H. Arakawa, J.L. Dubois, K. Sayama, *Energy Convers. Manage.* 33 (1992) 521–528.
- [15] M. Saito, T. Fujitani, I. Takahara, T. Watanabe, M. Takeuchi, Y. Kanai, K. Moriya, T. Kakumoto, *Energy Convers. Manage.* 36 (1995) 577–580.
- [16] M. Saito, T. Fujitani, M. Takeuchi, T. Watanabe, *Appl. Catal. A* 138 (1996) 311–318.
- [17] T. Inui, H. Hara, T. Takeguchi, J.-B. Kim, *Catal. Today* 36 (1997) 25–32.
- [18] J. Toyir, P.R.R. de la Piscina, J.L.G. Fierro, N.S. Homs, *Appl. Catal. B* 29 (2001) 207–215.
- [19] J. Słoczyński, R. Grabowski, P. Olszewski, A. Kozłowska, J. Stoch, M. Lachowska, J. Skrzypek, *Appl. Catal. A* 310 (2006) 127–137.
- [20] Y. Ma, Q. Sun, D. Wu, W.-H. Fan, Y.-L. Zhang, J.-F. Deng, *Appl. Catal. A* 171 (1998) 45–55.
- [21] J. Słoczyński, R. Grabowski, A. Kozłowska, P. Olszewski, J. Stoch, J. Skrzypek, M. Lachowska, *Appl. Catal. A* 278 (2004) 11–23.
- [22] F. Arena, K. Barbera, G. Italiano, G. Bonura, L. Spadaro, F. Frusteri, *J. Catal.* 249 (2007) 185–194.
- [23] R. Yang, Y. Fu, Y. Zhang, N. Tsubaki, *J. Catal.* 228 (2004) 23–35.
- [24] R. Yang, Y. Zhang, Y. Iwama, N. Tsubaki, *Appl. Catal. A* 288 (2005) 126–133.
- [25] R. Yang, X. Yu, Y. Zhang, W. Li, N. Tsubaki, *Fuel* 87 (2008) 443–450.
- [26] G. Bonura, M. Cordaro, C. Cannilla, F. Arena, F. Frusteri, *Appl. Catal. B* 152–153 (2014) 152–161.
- [27] T. Fujitani, J. Nakamura, *Appl. Catal. A* 191 (2000) 111–129.
- [28] L. Fan, K. Fujimoto, *Appl. Catal. A* 106 (1993) L1–L7.
- [29] T. Fujitani, M. Saito, Y. Kanai, T. Watanabe, J. Nakamura, T. Uchijima, *Appl. Catal. A* 125 (1995) L199–L202.
- [30] C. Shao, L. Fan, K. Fujimoto, Y. Iwasawa, *Appl. Catal. A* 128 (1995) L1–L6.
- [31] L. Fan, K. Fujimoto, *Energy Convers. Manage.* 36 (1995) 633–636.
- [32] T. Fujitani, I. Nakamura, *Bull. Chem. Soc. Jpn.* 75 (2002) 1393–1398.
- [33] S. Collins, D. Chiavassa, A. Bonivardi, M. Baltanás, *Catal. Lett.* 103 (2005) 83–88.
- [34] D.L. Chiavassa, J. Barrandeguy, A.L. Bonivardi, M.A. Baltanás, *Catal. Today* 133–135 (2008) 780–786.
- [35] X.-L. Liang, X. Dong, G.-D. Lin, H.-B. Zhang, *Appl. Catal. B* 88 (2009) 315–322.
- [36] M.L. Poutsma, L.F. Elek, P.A. Ibarbia, A.P. Risch, J.A. Rabo, *J. Catal.* 52 (1978) 157–168.
- [37] Y. Matsumura, W.-J. Shen, Y. Ichihashi, M. Okumura, *J. Catal.* 197 (2001) 267–272.
- [38] Y. Kikuzono, S. Kagami, S. Naito, T. Onishi, K. Tamaru, *Faraday Discuss. Chem. Soc.* 72 (1981) 135–143.
- [39] A. Gotti, R. Prins, *J. Catal.* 175 (1998) 302–311.
- [40] N. Koizumi, X. Jiang, J. Kugai, C. Song, *Catal. Today* 194 (2012) 16–24.
- [41] J. Nerlov, I. Chorkendorff, *Catal. Lett.* 54 (1998) 171–176.
- [42] J. Nerlov, I. Chorkendorff, *J. Catal.* 181 (1999) 271–279.
- [43] P.R. Subramanian, D.E. Laughlin, *J. Phase Equilib.* 12 (1991) 231–243.
- [44] P. Huang, S. Menon, D. Fontaine, *J. Phase Equilib.* 12 (1991) 3–5.
- [45] L. Lianos, Y. Debaughe, J. Massardier, Y. Jugnet, J.C. Bertolini, *Catal. Lett.* 44 (1997) 211–216.
- [46] L. Constant, P. Ruiz, M. Abel, Y. Robach, L. Porte, J.C. Bertolini, *Top. Catal.* 14 (2000) 125–129.
- [47] S. Sitthitha, T. Pham, T. Prasomsri, T. Sooknoi, R.G. Mallinson, D.E. Resasco, *J. Catal.* 280 (2011) 17–27.
- [48] J. Kugai, J.T. Miller, N. Guo, C. Song, *Appl. Catal. B* 105 (2011) 306–316.
- [49] J. Kugai, J.T. Miller, N. Guo, C. Song, *J. Catal.* 277 (2011) 46–53.
- [50] X.C. Xu, C.S. Song, J.M. Andresen, B.G. Miller, A.W. Scroni, *Energy Fuel* 16 (2002) 1463–1469.
- [51] X.X. Wang, V. Schwartz, J.C. Clark, X. Ma, S.H. Overbury, X.C. Xu, C.S. Song, *J. Phys. Chem. C* 113 (2009) 7260–7268.
- [52] X. Ma, X. Wang, C. Song, *J. Am. Chem. Soc.* 131 (2009) 5777–5783.
- [53] J. Kugai, J.T. Miller, N. Guo, C. Song, *Appl. Catal. B* 105 (2011) 306–316.
- [54] Y. Yang, M.G. White, P. Liu, *J. Phys. Chem. C* 116 (2012) 248–256.
- [55] M. Hsieh, T. Whang, *Appl. Surf. Sci.* 270 (2013) 252–259L.
- [56] X.L. Zhang, W.P. Wang, J. Liu, S.S. Sheng, G.X. Xiong, W.S. Yang, *Thin Solid Films* 516 (2008) 1849–1856.
- [57] A. Rochefort, M. Abon, P. Delichere, J.C. Bertolini, *Surf. Sci.* 294 (1993) 43–52.
- [58] A.M. Venezia, L.F. Liotta, G. Deganello, Z. Schay, L. Gucci, *J. Catal.* 182 (1999) 449–455.
- [59] E.B. Fox, S. Velu, M.H. Engelhard, Y. Chin, J.T. Miller, J. Kropf, *J. Catal.* 260 (2008) 358–370.
- [60] W.J. Shen, Y. Matsumura, *Phys. Chem. Chem. Phys.* 2 (2000) 1519–1522.
- [61] R. Gopinath, N. Lingaiah, B. Sreedhar, I. Suryanarayana, P.S.S. Prasad, A. Obuchi, *Appl. Catal. B* 46 (2003) 587–594.
- [62] D. Briggs, in: M.P. Seah (Ed.), *Practical Surface Analysis: Auger and X-Ray Photoelectron Spectroscopy*, Wiley, 1990.
- [63] J. Batista, A. Pintar, D. Mandrino, M. Jenko, V. Martin, *Appl. Catal. A* 206 (2001) 113–124.
- [64] L.C. Grabow, M. Mavrikakis, *ACS Catal.* 1 (2011) 365–384.